Highly reversible Zn metal anode enabled by sustainable hydroxyl chemistry

Lin Ma[a,b,1,2] (ID), Jenel Vatamanu[a,1] (ID), Nathan T. Hahn[c], Travis P. Pollard[a] (ID), Oleg Borodin[a,2], Valeri Petkov[d], Marshall A. Schroeder[a], Yang Ren[e], Michael S. Ding[a], Chao Luo[f,g,2] (ID), Jan L. Allen[a] (ID), Chunsheng Wang[h], and Kang Xu[a,2] (ID)

Rechargeable Zn metal batteries (RZMBs) may provide a more sustainable and lower-cost alternative to established battery technologies in meeting energy storage applications of the future. However, the most promising electrolytes for RZMBs are generally aqueous and require high concentrations of salt(s) to bring efficiencies toward commercially viable levels and mitigate water-originated parasitic reactions including hydrogen evolution and corrosion. Electrolytes based on nonaqueous solvents are promising for avoiding these issues, but full cell performance demonstrations with solvents other than water have been very limited. To address these challenges, we investigated MeOH as an alternative electrolyte solvent. These MeOH-based electrolytes exhibited exceptional Zn reversibility over a wide temperature range, with a Coulombic efficiency > 99.5% at 50% Zn utilization without cell short-circuit behavior for > 1,800 h. More important, this remarkable performance translates well to Zn ∥ metal-free organic cathode full cells, supporting < 6% capacity decay after > 800 cycles at −40 °C.

Zn metal batteries | sustainable electrolyte design | high reversibility | solid electrolyte interphase

Among the emerging battery chemistries beyond Li, rechargeable Zn metal batteries (RZMBs) have attracted intense interest due to the unique advantages of Zn metal, including higher abundance than Li (in moles of atoms) in the Earth's crust based on currently exploitable deposits in several key countries including the United States, Australia, and China (1); low toxicity; and superior volumetric capacity (5,854 Ah L^{-1} for Zn vs. 2,061 Ah L^{-1} for Li) (2, 3). However, the development of RZMBs has been plagued by challenges common to all metallic anodes, which include irreversible reactions such as hydrogen evolution, incessant consumption of active and electrolyte materials as indicated by the inferior plating/stripping Coulombic efficiency (CE), and the concomitant formation of undesired morphologies such as dendrites and electrochemically "dead" metal particles (4–6).

Several strategies have been proposed to address Zn irreversibility, including electrolyte engineering (7–16), artificial interphases (17, 18), and Zn electrode structure optimization (19, 20). As one of the most accessible aspects of battery manufacturing, electrolyte engineering is especially attractive. Relying on knowledge learned from Li–ion battery electrolyte design (21–23), tuning Zn^{2+} cation solvation structure by optimizing electrolyte formulations has become a critical and ubiquitous approach to improving Zn anode reversibility, which is especially effective in the case of aqueous electrolytes due to the ability to alter both interfacial structures and solid electrolyte interphase (SEI) chemistries via solvation structures. The emerging superconcentrated "water-in-salt" electrolytes offer opportunities to stabilize the Zn metal anode with a significant amount of salt anions (e.g., > 7 m Cl$^-$ [7, 8], 20 m bis(trifluoromethylsulfonyl)imide [TFSI$^-$] [9]) to partially replace H$_2$O in the Zn^{2+} solvation sheath, thus suppressing hydrogen evolution, promoting desired Zn–deposition morphology, and improving CE. The introduction of ionic liquid (e.g., acetamide-Zn(TFSI)$_2$ [10], urea/LiTFSI/Zn[TFSI]$_2$ [11]) or nonaqueous solvents (e.g., trimethyl phosphate-ethyl methyl carbonate [12], succinonitrile [13]) also provides an effective tactic to engineer the Zn^{2+} solvation sheath and SEI chemistry, thus improving Zn reversibility. However, despite the tremendous efforts devoted to developing advanced electrolytes for RZMBs from the perspective of solvation structure design, there are still many unanswered questions regarding the intricate correlation between the electrolyte structure, dynamics, SEI chemistries, and Zn reversibility. Equally important is to avoid the use of high-cost chemicals and electrolytes that support only limited Zn utilization per cycle (< 10%) (7–13, 15, 16), which remains far from the goal for a commercialized metal battery anode (5 mAh cm^{-2}, 10 mA cm^{-2}, 80% Zn utilization per cycle).(24, 25)

Here, we introduce a class of nonaqueous but protic electrolytes along with the associated hydroxyl-based interphasial chemistry. These electrolytes based on the alcohol

Significance

A rechargeable Zn metal battery (RZMB) is considered a technology of significance that could eliminate the supply chain and cost crisis brought by Li-based chemistries while maintaining comparable energy. However, current Zn metal electrodes are limited to shallow cycling conditions (< 1 mAh cm^{-2}) and inefficient utilization (< 10%) because of Zn irreversibility in battery environments. We used MeOH to alter the solvation structure of Zn electrolytes and interphasial chemistries and achieved high utilization (50%) and high Coulombic efficiency (99.5%) of a Zn metal electrode as well as an unprecedented wide service temperature range for the RZMB, down to −40°C. This work opens up a way to tailor the electrochemical behavior of Zn on the molecular level so that emerging battery chemistries can be realized for practical applications.

family, such as MeOH, are renewable solvents that can be generated at high efficiency from methane (a greenhouse gas) by bacteria (26). Like many solvents, the Zn^{2+} cation solvation structure can be tuned by adjusting the Zn salt (zinc trifluoromethanesulfonate [$Zn(OTf)_2$] as an example salt) concentrations in MeOH, thus affecting the degree of ion pairing and OTf^- anion decomposition. Interestingly, despite the observed differences in interphasial chemistry and thickness caused by salt concentration, these electrolytes enable extraordinary Zn reversibility over all tested concentrations at room temperature: a high CE (> 99.5%) with 50% Zn utilization per cycle and long-term cycling (> 1,800 h) without cell short-circuit behavior even under aggressive cycling conditions (2.5 mA cm^{-2}, 2.5 mAh cm^{-2}), which is a clear indication of the critical role played by the alcohol solvent in ensuring the high Zn reversibility and a welcome trend of gaining cost independence from the expensive salts. This work also establishes initial benchmarks toward supporting highly efficient Zn plating/stripping with a Zn utilization per cycle far beyond state-of-the-art Zn electrolyte efforts (*SI Appendix*, Table S1), especially including other alcohol-containing but still aqueous electrolytes. In addition to circumventing the salt cost, the dilute electrolyte composition also provides favorable transport properties that support high performance (CE > 99.5% with 20% Zn utilization), even at extreme temperatures at −40 °C. These results open an alternative direction into achieving a low-cost, sustainable, and high-performance battery chemistry by leveraging the correlation between local intermolecular interactions, bulk transport properties, and interphasial chemistries.

Results

Bulk Solvation and Transport properties.
A wide range of $Zn(OTf)_2$ salt concentrations in MeOH (111:1, 23:1, and 14:1, denoting MeOH:$Zn(OTf)_2$ by mol) was explored using several spectroscopic methods in combination with molecular dynamics (MD) simulations. In the Raman spectra (Fig. 1 *A–C*), a broad OTf^- anion S–O symmetric stretching band was assigned to the solvent-separated ion pairs (SSIP) at 1,032 to 1,034 cm^{-1} and contact ionic pairs (CIP) at 1,042 cm^{-1} following previous reports (27, 28). The deconvolution of these bands revealed an increase in the fraction of CIPs (*SI Appendix*, Fig. S1) from less than 10% for a 111:1 salt concentration to ~30% at a 14:1 salt concentration. To complement the Raman testing, dielectric relaxation spectroscopy (DRS) was also used to investigate the electrolyte structures. The increase in the $Zn(OTf)_2$ salt concentration led to a decrease in the electrolyte dielectric constant (static permittivity at low frequency) as shown in the relative permittivity spectra (Fig. 1*D* and *SI Appendix*, Fig. S2), which suggests the rotational freezing of a large fraction of MeOH solvent due to Zn^{2+} solvation (29). Corresponding dielectric loss spectra exhibited three distinct relaxations (*SI Appendix*, Fig. S3) that were attributed to ionic pairs (including both SSIP and CIP, ~1 GHz), cooperative (strong H-bonded) MeOH solvent motion (~2.5 GHz), and noncooperative solvent motion (~9 GHz). Combined with the Raman results, the decrease in the ionic pair contribution to the dielectric constant between 111:1 and 23:1 suggests a shift from SSIP to CIPs, which have a smaller dipole moment. The increasing salt concentration also suppressed the hydrogen-bonding network, as indicated by an increase in noncooperative MeOH contribution. This conclusion was further supported by the presence of more definite features at a higher wavenumber (~3,500 cm^{-1}, indicated by a yellow square in Fig. 1*E*) in the broad O–H stretching band of the Fourier transform infrared (FTIR) spectra and the MD simulation results (*SI Appendix*, Table S2). MD simulations showed an excellent agreement with experiments for the MeOH dielectric loss spectrum (*SI*
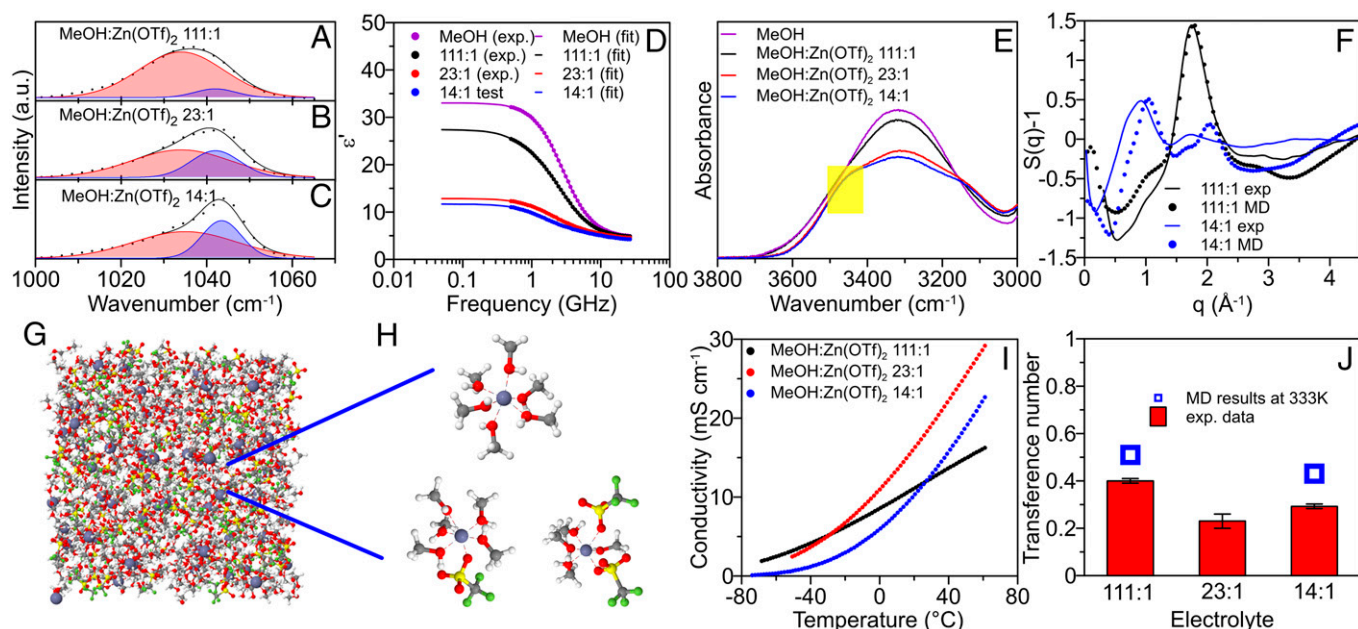

Fig. 1. Bulk and transport properties of MeOH-based electrolytes. (*A* and *B*) The Raman spectra of the S–O symmetric stretching band of OTF$^-$ in (*A*) 111:1, (*B*) 23:1, and (*C*) 14:1 electrolytes, respectively. Experimental spectra (dots) were deconvoluted using Gaussian function (solid line). Red peak: SSIP; blue peak: CIP. (*D*) The experimental real permittivity spectra (dots) for selected electrolytes measured using DRS at room temperature and their corresponding fitted lines (solid line). (*E*) The FTIR spectra of the O–H band. The yellow square indicates the region with higher wavenumber (~3500 cm^{-1}). (*F*) The experimental synchrotron X-ray scattering curve (solid line) and the MD simulation (at 298K) line (dashed line). (*G* and *H*) Snapshots of the MD simulation box (at 333K) for (*G*) the 14:1 electrolyte and (*H*) its clusters collected from MD. Note that the cluster of ($Zn(OTf)_2(MeOH)_4$) is less frequent than the cluster of ($ZnOTf(MeOH)$)$^+$. (*I*) Temperature-dependent conductivities for MeOH-based electrolytes. (*J*) Summary of Zn^{2+} transference number in MeOH-based electrolytes measured using the steady-state galvanostatic polarization method. Open squares indicate MD calculated values (at 333K) using the Rolling method.

Appendix, Fig. S4), a sharp drop in the dielectric strength of MeOH from 34 in pure MeOH to 12 in 14:1 electrolyte due to a disruption of the hydrogen bonding network and less dielectrically active $Zn(MeOH)_n$ solvate formation. Moreover, the MeOH phase in 14:1 electrolyte showed a broader spectrum with both a faster and slower relaxation than pure MeOH, suggesting that both high- and low-frequency components of the experimentally observed dielectric loss are, at least partially, due to the MeOH phase in $MeOH:Zn(OTf)_2$ 14:1.

Synchrotron X-ray scattering measurements were performed for pure MeOH (as a standard sample; *SI Appendix,* Fig. S5) as well as 111:1 and 14:1 electrolytes to validate the intermediate-range electrolyte structures predicted by MD simulations (Fig. 1*F* and *SI Appendix,* Fig. S5). The good agreement between calculated and experimental structure factors S(q) suggests that the applied force field can reproduce the local structure of this system over a wide range of $Zn(OTf)_2$ concentrations in MeOH. In particular, the first intermolecular peak position change (from 1.9 $Å^{-1}$ to 1.0 $Å^{-1}$) and shape change, caused by the addition of salt from 111:1 to 14:1 electrolyte, were accurately predicted by the MD simulations. The peak shift was attributed to the changes of MeOH packing from the hydrogen-bonded MeOH to $Zn(MeOH)_6$ and anion ordering. In the 111:1 electrolyte, more than 90% of the Zn^{2+} cations were fully solvated by MeOH molecules according to MD simulations (*SI Appendix,* Fig. S6), which gave rise to $(Zn(MeOH)_6)^{2+}$ cations (*SI Appendix,* Fig. S7). Such cation–solvent interactions could result in a significantly weakened O–H bond within a MeOH molecule and generate a mildly acidic environment (*SI Appendix,* Fig. S8). With an increasing $Zn(OTf)_2$ concentration, the fraction of $(Zn(OTf)(MeOH)_5)^+$ CIP increased up to ~26% in the 14:1 electrolyte (Fig. 1 *G* and H and *SI Appendix,* Fig. S6), which was consistent with Raman and DRS results (Fig. 1 *A–D*).

The temperature dependence in ionic conductivity for the 111:1, 23:1, and 14:1 electrolytes is shown in Fig. 1*I*. Above −20 °C, the 23:1 electrolyte at an intermediate salt concentration demonstrated the highest conductivity thanks to the optimum contributions from both ion carrier number and ion dissociation; such behavior has been observed for many electrolytes (30). An adequate agreement existed between MD predictions and experimental conductivity results (*SI Appendix,* Table S3). There was also a reasonable agreement between the MD simulation results (*SI Appendix,* Table S3) and experimental results on other dynamics properties of the electrolytes, including Zn^{2+} transference number (Fig. 1*J* and *SI Appendix,* Fig. S9) and viscosity (*SI Appendix,* Fig. S10).

Zn Metal Anode Reversibility. The Zn plating/stripping reversibility was then evaluated in these electrolytes with different salt concentrations and corresponding solvation structures. During the screening stage, Zn plating/stripping CE, which is a critical figure-of-merit for Zn reversibility, was measured using an established galvanostatic protocol (31) with an anodeless Cu|Zn (100 μm) cell setup at room temperature. Despite the differences in the Zn^{2+} solvation sheath compositions at different concentrations, the average CEs (*SI Appendix,* Fig. S11) were all above 99.5% for these electrolytes, which predicts high electrochemical reversibility. A more rigorous evaluation of the CE using a "reservoir-free" galvanostatic protocol (*SI Appendix,* Fig. S12) was applied to Cu|Zn (10 μm) cell setups under more aggressive conditions (2.93 mA cm^{-2}, 2.93 mAh cm^{-2}, 50% Zn utilization per cycle). Intriguingly, an average CE above 99.9% (Fig. 2 *A–C*) with a low Zn plating overpotential (<0.1 V) was achieved for all three electrolytes after 140 cycles (280 h), which suggests that

they are equally promising systems to prevent interphasial side reactions and support high energy–density RZMBs. Such an extraordinary performance could not even be achieved by the state-of-art nonaqueous Zn–ion electrolyte based on triethyl phosphate (15) (*SI Appendix,* Fig. S13). Afterward, these MeOH electrolytes were also tested in a Zn|Zn (100 μm) symmetric cell setup under aggressive galvanostatic conditions (1 mA cm^{-2}, 1 mAh cm^{-2}; 2.5 mA cm^{-2}, 2.5 mAh cm^{-2} and 1 mA cm^{-2}, 5 mAh cm^{-2}) to examine their capability in suppressing dendrite formation/growth and excessive impedance growth during long-term cycling at room temperature (Fig. 2 *D–F* and *SI Appendix,* Figs. S14 and S15). All electrolytes were found to generate dendrite-free morphologies and excellent long-term cycling stability with a low overpotential (<0.1 V) after 1,800 h of cycling (Fig. 2 *D–F* and *SI Appendix,* Fig. S15).

Zn reversibility in these electrolytes was also explored at the extreme temperature of −40 °C. In a Cu|Zn (10 μm) cell setup under harsh testing conditions (1.17 mA cm^{-2}, 1.17 mAh cm^{-2}, 20% Zn utilization per cycle), the 23:1 and 14:1 electrolytes failed (*SI Appendix,* Figs. S16 and S17) and exhibited large overpotentials, which could be due to transport limitations at a low temperature (Fig. 1*I* and *SI Appendix,* Fig. S18*A*). In contrast, Zn anodes demonstrated superior plating/stripping reversibility in the 111:1 electrolyte (Fig. 2*G*) with an average CE above 99.5% after 270 cycles (540 h). The stabilization of CE at the initial process could be due to the evolution of interphase as indicated by electrochemical impedance spectroscopy (EIS) results (*SI Appendix,* Fig. S18 *B–D*) and is discussed in the next section. This result encourages the application of MeOH-based RZMBs in the field of low-temperature energy storage (*SI Appendix,* Table S1).

Postcycling Analysis. To understand the mechanism behind the exceptional electrochemical performance, interphasial characterization was conducted. When we recovered ecovering cycled electrodes from both 111:1 and 14:1 electrolytes, we meticulously studied and compared the Zn metal morphology and SEI structures/chemistries. Fig. 3 *A–D* show focused ion beam–scanning electron microscopy (FIB-SEM) images with cross-sectional views of Zn metal electrodes from 111:1 (Fig. 3 *A* and *B*) and 14:1 (Fig. 3 *C* and *D*) electrolytes after 20 h (Fig. 3 *A* and *C*) and 200 h (Fig. 3 *B* and *D*) cycling at 2.5 mA cm^{-2}, 2.5 mAh cm^{-2} per cycle. In general, regardless of the electrolyte composition, the images captured a textured but nondendritic morphology at a selected cycling stage, which aligned well with the cycling data.

Transmission electron microscopy (TEM) and X-ray photoelectron spectroscopy (XPS) combined with density functional theory (DFT) calculations were utilized to analyze the evolution of interphasial structures and chemistries with cycling time. The carbon layers seen in all TEM images (Fig. 3 *E–H*) were artificially coated prior to TEM sample preparation to protect the formed interphase during the FIB cutting process. After a very short-term (20 h) cycling period, a uniform ~4 to 10 nm interphase layer could be observed for both the 111:1 (Fig. 3*E*) and 14:1 electrolytes (Fig. 3*G*). XPS depth profiling showed clear F 1s and S 2p depth profile for 14:1 electrolytes (*SI Appendix,* Figs. S19 and S20), which suggests that the OTf^- anion decomposition (main products including ZnS, $ZnSO_3$, and ZnF_2) is facilitated by an enrichment of the OTf^- anion in the electric double layer (EDL, *SI Appendix,* Fig. S21). Interestingly, this occurred despite the unfavorable electrochemical reduction potential for the OTf^- anion compared to the H_2 evolution from MeOH (*SI Appendix,* Fig. S22 and S23). By comparison,
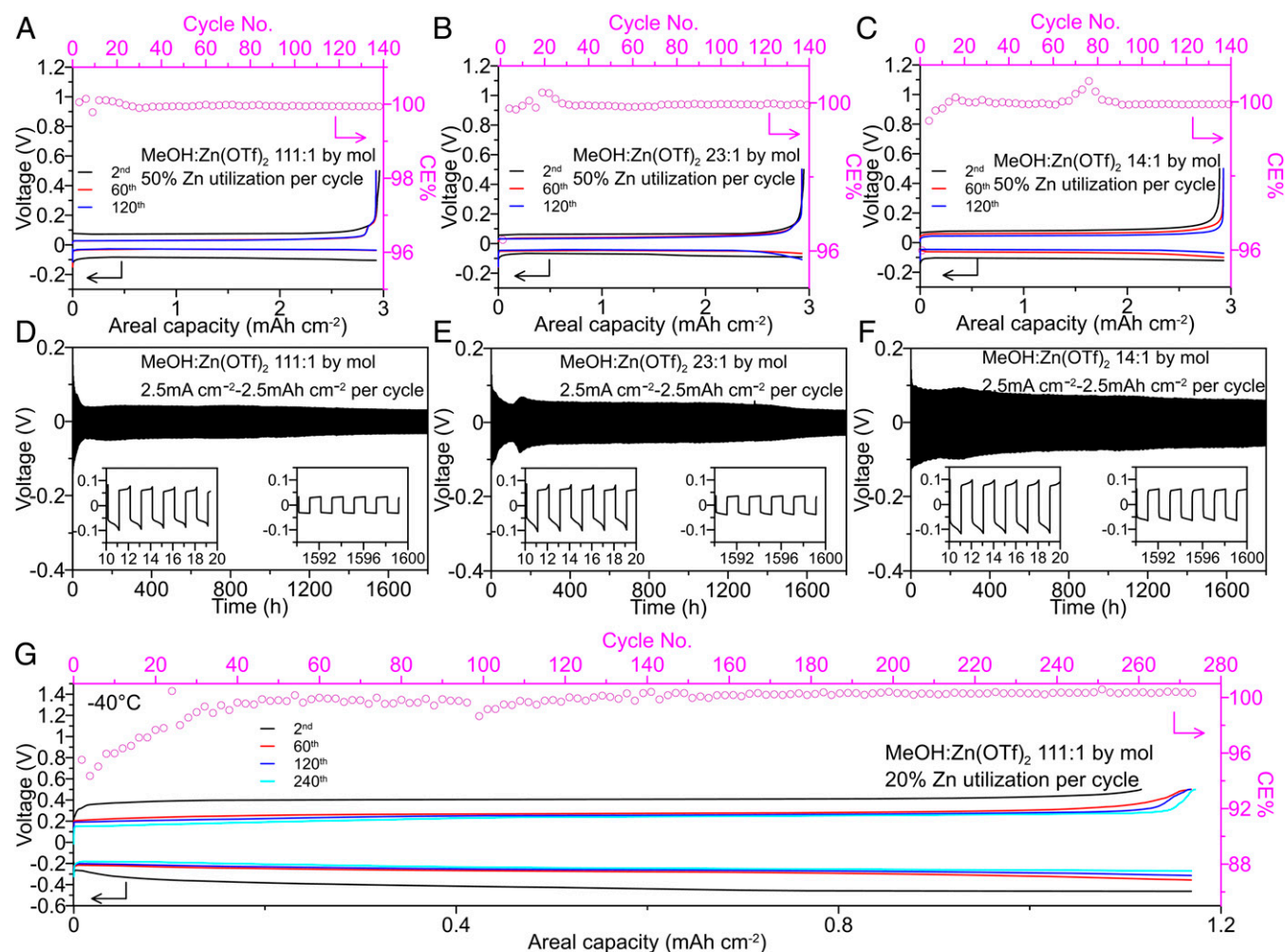
Fig. 2. Zn metal anode electrochemical reversibility in MeOH-based electrolytes. (*A–C*) Zn plating/stripping profiles and corresponding CE cycled in (*A*) 111:1, (*B*) 23:1, and (*C*) 14:1 electrolyte, respectively, using a Cu|Zn (10 μm) cell setup at room temperature and 2.93 mA cm^{-2} to an areal capacity of 2.93 mAh cm^{-2} per cycle. (*D* and *E*) Galvanostatic Zn plating/stripping cycled in (*D*) 111:1, (*E*) 23:1, and (*F*) 14:1 electrolyte, respectively, using a Zn|Zn(100 μm) cell setup at room temperature with 2.5 mA cm^{-2} to an areal capacity of 2.5 mAh cm^{-2} per cycle. (*G*) Zn plating/stripping profiles and corresponding CE cycled in 111:1 electrolyte using Cu|Zn(10 μm) cell setup at −40 °C and 1.17 mA cm^{-2} to an areal capacity of 1.17 mAh cm^{-2} per cycle.

these products were barely detected in the XPS spectra for the samples recovered from the highly dissociated 111:1 electrolyte (*SI Appendix,* Fig. S24). When we extended the cycling time up to 200 h, the SEI thickness increased compared to that in the electrodes cycled for 20 h (Fig. 3 *F* and *H*). In addition, the F 1s signal and S 2p signal (*SI Appendix,* Figs. S25 and S26) in the XPS spectra, as well as the results from energy-dispersive X-ray spectroscopy for F and S (*SI Appendix,* Figs. S27 and S28), were obtained for both the 111:1 and 14:1 electrolytes. This suggests that OTf$^-$ anions could also decompose through other routes during long-term cycling, even in the diluted 111:1 electrolyte. These reactions could occur via nucleophilic attack reaction by bases (16) (e.g., methoxide generated at the Zn anode surface [Fig. 3*M* and *SI Appendix,* Fig. S29]) or electrochemical reduction under locally higher overpotentials at ZnO nanodomains (*SI Appendix,* Fig. S30).

Considering the concentration-dependent variation in interphasial chemistry, salt concentration and the fraction of anion-derived SEI did not seem to be the critical factor supporting the consistently excellent Zn reversibility for both the 111:1 and 14:1 electrolytes, in contrast with the aqueous electrolytes that rely on both. To further explore this hypothesis, DFT calculations were used to examine potential reaction mechanisms of MeOH solvent on the Zn surface. The deprotonation reaction

(Fig. 3*M*) in the presence of ZnO on the Zn surface (*SI Appendix,* Fig. S31) was highly favorable, during which the preferred products were $Zn(OH)_2$ and $Zn(OCH_3)_2$. $Zn(OH)_2$ formation was also favorable from the $Zn^{2+}(MeOH)_6$ reduction when the dissolved O_2 was present in electrolyte (*SI Appendix,* Fig. S23), in accord with a previous report (32). The XPS spectra of O 1s (Fig. 3 *I–L*) further supported this argument by showing these products [$Zn(OH)_2$ (33–35) and $Zn(OCH_3)_2$] for both the 111:1 and 14:1 electrolytes spanning a 20 h and 200 h cycling time range. The presence of this $Zn(OH)_2$-containing interphase was also evidenced by X-ray diffraction (XRD) (*SI Appendix,* Fig. S32), which showed a broad peak centered near 20° two-theta that matched the position of the most intense XRD peaks of $Zn(OH)_2$ (PDF#01–089-0138). The extremely broad peak is characteristic of the nanoscale dimensions of interphase. Such protonation behavior on ZnO has been reported to decrease electronic conductivity by creating a depletion region around the ZnO grains and to enhance ionic conductivity by providing preferential channels (grain boundaries parallel to the electric field) for ionic percolation (36). Here, regardless of the different electrolyte solvation structures, ZnO protonated by methanol could generate benign interphasial chemistry, suppressing both parasitic reactions via less electronic conductivity and the prevention of dendrite formation/growth via enhanced ionic conductivity, thus
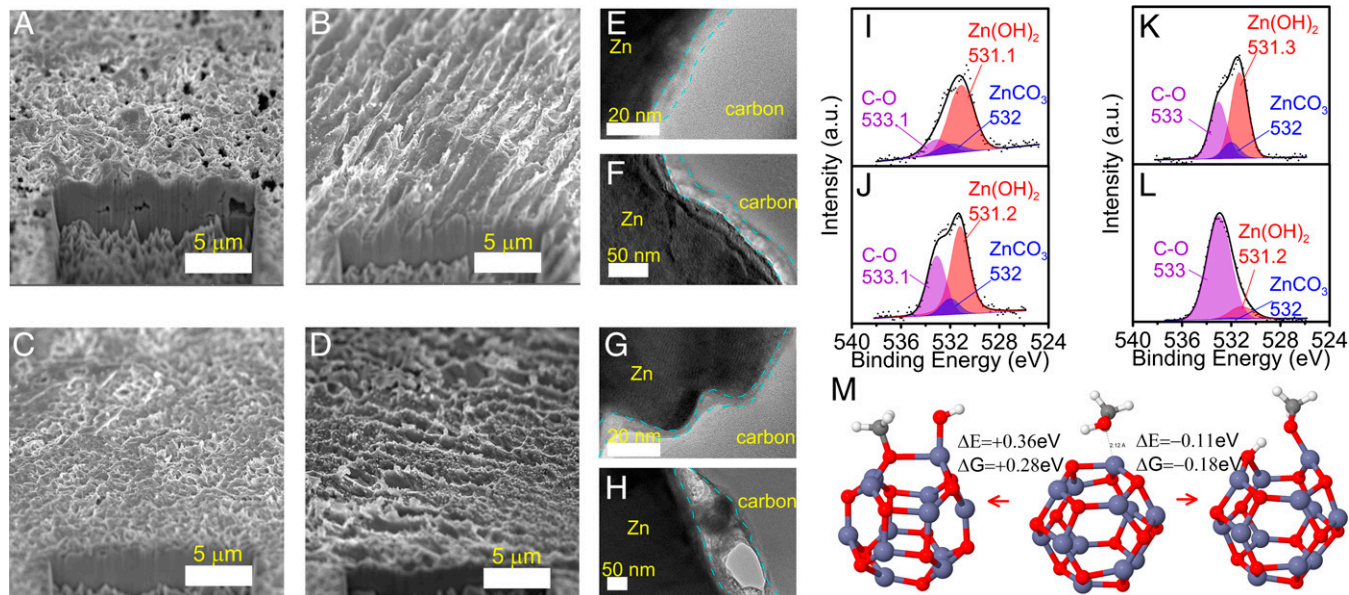
Fig. 3. Postcycling analysis of Zn metal anode. (A and B) FIB-SEM images of Zn metal anode obtained from Zn|Zn (100 μm) symmetric cells at a zero state of charge after (A) 20 h and (B) 200 h cycling (2.5 mA cm⁻², 2.5 mAh cm⁻² per cycle) with 111:1 electrolyte at room temperature. (C and D) FIB-SEM images of Zn metal anode obtained from Zn|Zn (100 μm) symmetric cells at a zero state of charge after (C) 20 h and (D) 200 h cycling (2.5 mA cm⁻², 2.5 mAh cm⁻² per cycle) with 14:1 electrolyte at room temperature. (E and F) TEM images of Zn metal anodes corresponding to (A) and (B), respectively. (G and H) TEM images of Zn metal anodes corresponding to (C) and (D), respectively. The interphasial region is labeled by blue dashed lines. (I and J) XPS spectra of O 1s for Zn metal anodes corresponding to (A) and (B), respectively. (K and L) XPS spectra of O 1s for Zn metal anodes corresponding to (C) and (D), respectively. The O 1s peak position assignment can be referred to C–O (~533 eV) (33, 34), ZnCO₃ (~532 eV) (16), and Zn(OH)₂ (~531 eV) (35). (M) wB97XD/6–31+G(d,p) DFT calculation results on the decomposition process of MeOH on the nanoscale ZnO cluster distributed on the Zn metal surface. H: white; O: red; Zn: blue gray; C: light gray.

homogenizing the surface electric field. The presence of $ZnCO_3$ on the Zn surface (SI Appendix, Fig. S31) and its retention during cycling (Fig. 3 I–L) may also play a role in suppressing Zn dendrite growth according to a previous report (16) due to its higher shear modulus compared to Zn. The robustness of the interphase thus formed was further confirmed by demonstrating a lack of aging/corrosion current (SI Appendix, Fig. S33), indicating an excellent storage lifetime (> 400 h) of Zn metal in these electrolytes. The improvements in Zn reversibility were also observed for ethanol-based electrolytes (SI Appendix, Fig. S34), which was attributed to the same interphase formation mechanism (SI Appendix, Fig. S35). However, the presence of greater than ppm amounts of water may compromise the quality of the interphase (SI Appendix, Fig. S36), due to excessive water decomposition and/or zincate/ZnO formation.

Full Cell Performance Demonstration. The performance of the 111:1 and 14:1 electrolytes was further demonstrated in a full cell consisting of a metal-free organic cathode based on polyaniline (PANI; ~7 mg cm⁻²) and a thin Zn anode (10 μm thickness, ~7.14 mg cm⁻²), aiming to develop cost-effective and sustainable RZMBs. Fig. 4A shows that ~80% of the maximum capacity was retained after ~280 cycles in the 111:1 electrolyte when the cell was tested at 60 mA g⁻¹ (corresponding to the PANI active material mass) between 0.4 V and 1.4 V at 30 °C. Note that the CE of the 111:1 electrolyte (Fig. 4A) was inferior compared to that of the 14:1 electrolyte (Fig. 4B) during cycling, which could be attributed to the difference in the anodic stability on the cathode surface (SI Appendix, Fig. S37). Consequently, the 14:1 electrolyte demonstrated a longer cycling lifetime (~90% capacity retention of maximum capacity after ~400 cycles) under the same testing condition (Fig. 4B). In the case of the 14:1 electrolyte, there was initially an increasing trend in capacity, different from the 111:1 electrolyte. Since the PANI cathode chemistry works with a dual-ion (both Zn^{2+} cation and

OTf⁻ anion) storage mechanism (37), the higher fraction of CIP in the 14:1 electrolyte could have slower kinetics on decoupling the Zn^{2+} cation and OTf⁻ anion compared to a highly dissociated solvation structure (111:1 electrolyte). When increasing the current density up to 360 mA g⁻¹ (Fig. 4 C and D), a high-discharge specific capacity could still be obtained for both the 111:1 (85 mAh g⁻¹, 80% of that of 60 mA g⁻¹) and 14:1 electrolyte (63 mAh g⁻¹, 82% of that of 60 mA g⁻¹). Overall, this PANI/Zn full cell demonstration achieved an energy density of 158 Wh L⁻¹ (SI Appendix, Table S4), corresponding to ~15% Zn utilization per cycle (SI Appendix, Fig. S38). This is an encouraging result for a Zn electrolyte based purely on a nonaqueous solvent chemistry. In addition, this electrolyte's ability to support reversible Zn anode cycling at 50% utilization per cycle suggests promise toward supporting RZMBs with much higher energy density when paired with higher cathode loadings or cathode materials with higher specific capacity/voltage (38).

The extraordinary Zn metal reversibility observed for the 111:1 electrolyte at a low temperature was also tested in this PANI/Zn full cell configuration with 60 mA g⁻¹ at −40 °C. When the cell was cycled between 0.4 V and 1.4 V, almost no capacity could be delivered (SI Appendix, Fig. S39), likely due to the higher overpotential at low temperatures (Fig. 2G). However, by increasing upper cutoff voltage to 1.8 V, a stable long cycling lifetime (~800 cycles) was achieved with ~95% of the maximum capacity (~85 mAh g⁻¹) retention (Fig. 4E), demonstrating great promise for the application under extreme conditions.

Discussion

Despite efforts to design advanced electrolytes for reversibly cycling Zn metal, these systems still fail to support commercially relevant targets for current density, areal capacity, Zn utilization per cycle, and cycle lifetime, not to mention the additional constraints from cost and sustainability.
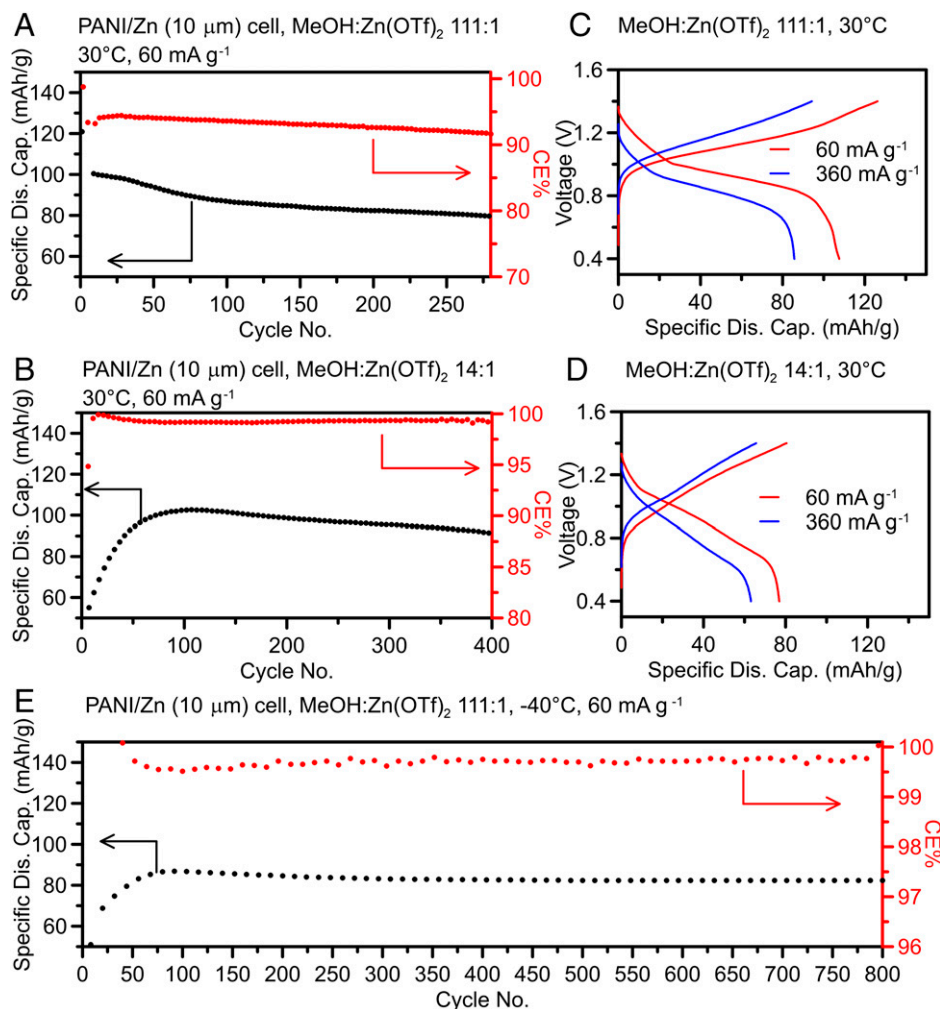
Fig. 4. Full cell performance demonstration of MeOH-based electrolytes. (*A*) CE and corresponding specific discharge capacity vs. cycle number for 111:1 electrolyte tested with PANI ($\sim$7 mg cm^{-2})|Zn(10 μm) cell setup at 60 mA g^{-1} (based on the mass of PANI) between 0.4 and 1.4 V at 30 °C. (*B*) CE and corresponding specific discharge capacity vs. cycle number for 14:1 electrolyte using the same cell setup and condition as in (*A*). (*C* and *D*) Charge–discharge profile (seventh cycle) corresponding to the cell setup and electrolytes in (*A*) and (*B*), respectively, at 60 mA g^{-1} and 360 mA g^{-1} at 30 °C. (*E*) CE and corresponding specific discharge capacity vs. cycle number for 111:1 electrolyte tested with PANI ($\sim$7 mg cm^{-2})|Zn(10 μm) cell setup at 60 mA g^{-1} (based on the mass of PANI) between 0.4 and 1.8 V at −40 °C.

In the current work, we have broadened the classical electrolyte design strategy by identifying MeOH as a cost-effective (*SI Appendix,* Table S5) and sustainable solvent and explored its ability to support these aggressive conditions. By adjusting the Zn(OTf)$_2$ salt concentrations in MeOH, we created a series of electrolytes with different Zn^{2+} cation solvation structures, which were rigorously studied with FTIR, Raman, DRS, synchrotron X-ray scattering, and MD simulation. Distinctly differing from previous efforts in which Zn anode reversibility was highly dependent on salt concentration and the subsequent solvation structures, electrolytes with different solvation structures in this work showed little impact on electrochemical performance. Instead, extraordinary Zn reversibility was achieved over a wide range of concentrations, with a Zn stripping/plating CE > 99.5% without cell short-circuit behavior even at an unprecedented 50% Zn utilization per cycle over long-term cycling (>1,800 h). This is attributed to the participation of MeOH in the interphasial chemistries through (Zn(MeOH)$_6$)$^{2+}$ reduction when O$_2$ is present and MeOH deprotonation to ZnO as suggested by XPS measurements and DFT calculations. At low temperatures (approximately −40 °C), the advantage of dilute electrolytes became pronounced over the concentrated electrolytes due to the differences in both bulk and interphasial transport properties.

Using a template cathode material (PANI) and a limited Zn anode, this stable reversibility was also demonstrated in full cells with excellent capacity retention during long-term cycling at both 30 °C and −40 °C.

This work highlights the importance of tailoring interphasial chemistries in addition to the conventional approach of focusing on bulk transport properties across a broad temperature range. Further exploration of these insights with sustainable materials should lead to significant improvements, which include extending the Zn anode lifetime, adapting to Mn-based cathode material (*SI Appendix,* Fig. S41), and using other OH-functionalized solvents and Zn salts, as we have separately demonstrated with ethanol (*SI Appendix,* Fig. S34) and a more sustainable salt-zinc acetate (Zn(Ac)$_2$) (*SI Appendix,* Fig. S40). Finally, appropriate molecular design and selection of cosolvents (e.g., water) or flame-retardant additives could eliminate flammability, yielding an electrolyte that can support each of the practical considerations for RZMBs: relatively low cost, safety, and sustainability.

Materials and Methods

Materials. Zn(OTf)$_2$ (98%) and EtOH (99.9%, water content 40 ppm) were purchased from Sigma-Aldrich. Anhydrous MeOH (99.9%, water content 78 ppm)

was purchased from Alfa Aesar. Zn foils with different thickness (10 μm [99.9%] and 100 μm [99.994%]) were purchased from Alfa Aesar. All the electrolyte solutions were formulated by dissolving Zn salts into solvents according to different concentrations in an Ar-filled glovebox. The cathode electrode material PANI was synthesized according to previous reports (37). Next, the PANI powders, Timical Super C45 (MTI) and PTFE (Sigma-Aldrich) ,were dispersed in anhydrous 2-propanol (99.5%; Sigma-Aldrich) with a mass ratio of 7:2:1. The slurry was then coated and calendared on a Ti mesh current collector and dried at room temperature overnight to remove 2-propanol. The loading of the PANI was ∼7 mg cm^{-2}.

Characterizations. Infrared spectra were collected for selected electrolyte samples using the average of 64 scans collected at a resolution of 2 cm^{-1}. The data were obtained using a Nicolet 6700 spectrometer (Thermo Scientific) equipped with a diamond attenuated total internal reflection setup. Raman spectra were collected for selected electrolyte samples using a Renishaw inVia Confocal Raman microscope equipped with a 532 nm near infrared laser. The measurement was carried out by focusing the laser light onto the electrolyte samples in a quartz nuclear magnetic resonance tube using a 20× objective lens. Each measurement was 6 s exposure in length and 10 accumulations. Spectra background subtraction was performed using Renishaw's Wire 2.0 software.

Synchrotron X-ray data for MeOH and Zn-containing electrolytes were obtained at the 11-ID-C beamline at the Advanced Photon Source, Argonne National Laboratory using high-energy (105.7 keV) X-rays with a wavelength of 0.1173 Å. Several scans were taken and averaged out to improve the statistical accuracy. The total measuring time amounted to 3 h per sample. An empty capillary was measured separately for 1 h to evaluate the background scattering due to the capillary and sample environment. Scattered intensities were recorded using a large area 2-dimensional detector and converted to the structure factors shown in Fig. 1F using well-established procedures (39).

DRS measurements were made in glass vials using a coaxial probe (Keysight N1501A) and a vector network analyzer (Keysight P9375A). Three-point calibration was performed using air, water, and tetrahydrofuran. Measurements were made over a frequency range of 0.5 to 26.5 GHz. The complex permittivity data (ε′ and ε″) and electrolyte conductivity were fit using three Debye relaxations with no parameter constraints. Due to distortions in the low frequency ε″ data resulting from high ionic conductivity, the lower frequency limit of the fitting window for ε″ was shifted from 0.5 GHz to slightly higher values (up to 1.0 GHz in the highest conductivity sample), as is typically performed in the literature (29, 40). Fitting parameters derived for the three electrolyte concentrations as well as pure MeOH are shown in the *SI Appendix*. The three Debye relaxations needed to accurately fit the permittivity spectra can be tentatively assigned to three different solution components based on their relaxation frequencies: MeOH (∼2.5 GHz), ion pairs (∼1 GHz), and an initially unexplained component at 7 to 10 GHz. While the assignments of MeOH and ion pairs were straightforward based on pure solvent measurements and typical ion pair behavior, the assignment of the highest frequency component was assisted via autocorrelation function analysis of the MD data. This analysis indicated that the high-frequency component is a fast, noncooperative MeOH relaxation that is related to disruption of the H-bonding network (41).

Electrolyte ionic conductivities were obtained based on the procedure in a previous report (14). Briefly, impedance scans were performed from 20 Hz to 2 MHz with an amplitude of 20 mV using an Agilent E4980A precision LCR (inductance, capacitance, and resistance) meter. A YSI 3418 cell was adapted to make it fit tightly into a polyethylene bottle for holding an electrolyte. The cell constant (0.1 cm^{-1} nominal) was calibrated with a 100 mS/cm standard solution. During the impedance scan, both the sample cell and the reference cell were ramped down from 60 to −70 °C, then back up at 0.1 °C min^{-1} in an environmental chamber (Tenney Jr.). The viscosity of electrolytes was determined using a Ostwald viscometer (Sibata, Japan) in a temperature-controlled water bath environment at 20 °C, 30 °C, 40 °C, and 50 °C, respectively. The fundamental electrolyte transport parameter of the transference number (t_+) was measured at each MeOH/Zn(OTf)$_2$ composition using symmetric Zn/Zn Swagelok cells. The two Zn electrodes consisted of planarized and freshly polished Zn rod faces (99.9%, Roto Metals) with diameters of 6.4 mm. Two Whatman GF/F glass microfiber discs saturated with electrolyte served as separators between the two rod faces. The actual compressed thickness of the total electrolyte/separator layer during the experiment was determined from the measured solution

resistance based on the known electrolyte conductivity as well as the porosity (0.89) and tortuosity (∼1.0) of the GF/F discs (42), yielding typical values of ∼500 μm. The polished Zn surfaces were further activated prior to each experiment using rapid galvanostatic cycling at 2 mA cm^{-2} to minimize interfacial impedance and promote uniform utilization of the Zn electrode area. Two cells were operated under each test condition and two measurements were made per cell (one in either polarization direction), for a total of four measurements per test condition. Measurements of t_+ were made using steady-state galvanostatic polarization of the cell at various current densities ranging from 2 to 6 mA cm^{-2} using a duration of 2 h. Under galvanostatic conditions, t_+ was derived from the initial (Φ_0) and steady-state (Φ_{ss}) potential drops across the electrolyte phase according to Eq. **1**.

$$\frac{\Phi_0}{\Phi_{ss}} = t_+. \tag{1}$$

In the initial condition, there is no concentration gradient across the electrolyte and Ohm's law applies (43), yielding Eq. **2**.

$$\Phi_0 = I \cdot R_s. \tag{2}$$

Here, R_s is the solution resistance measured by EIS just prior to polarizing the cell at current I. At the steady-state condition, the electrolyte potential drop is determined from Eq. **3** using the steady-state cell voltage (V_{ss}) corrected for the interfacial resistance ($R_{i,ss}$) measured by EIS at this condition. Example EIS profiles are shown in the *SI Appendix*.

$$\Phi_{ss} = V_{ss} - I \cdot R_{i,ss}. \tag{3}$$

The morphology of Zn metal electrodes was examined using a scanning electron microscope (SEM; Hitachi SU-70). The detailed interphasial morphology of selected Zn electrodes was studied using TEM (JOEL 2100F). All the TEM species were carefully prepared using an FIB (Tescan GAIA). An ∼100 nm thick carbon layer and a tungsten-containing protection layer were coated sequentially on the Zn sample surface before FIB cutting to protect its interphase. XPS measurements (PHI Versaprobe III) were conducted following the procedure described in the previous work (14). To avoid the potential air effect, Zn samples were collected from coin cells in an argon-filled glovebox, then rinsed with anhydrous acetonitrile and dried in an antechamber under vacuum overnight before transferring into the XPS system using a sealed vacuum transfer setup. The XPS measurements were carried out with a combination of survey scan (pass energy 224 eV, step size 0.4 eV) and high-resolution scan (pass energy 55 eV, step size 0.05 eV) during the surface-sputtering process. The X-ray focusing on a spot size of 100 μm was set with a power of 25 W. Surface neutralization was maintained by using a combination of a low-energy Ar–ion flow and an electron neutralizer. The Ar$^+$ sputtering beam was set as 500 V within a 3 mm × 3 mm region. During the spectra fitting process, all the spectra were shifted relative to the binding energy of 284.8 eV (C1s sp3) to compensate for any surface charging offset during the measurement. Using PHI's Multipak software version 9.6., the XPS spectra peak was fitted with 70/30 Gaussian/Lorentzian line shapes on a Shirley background. All the Zn electrode samples for SEM, TEM, and XPS characterization were obtained from Zn|Zn (100 μm) symmetric cells at a zero state of charge after certain period cycling with different current densities and areal capacities. XRD (Cu Kα radiation, Rigaku Miniflex 600, D/teX Ultra silicon strip detector, Rigaku Americas Inc., The Woodlands, TX) data were collected from 10 to 70° 2θ at 0.02° increments at 4° per minute to characterize the Zn electrode. Additional characterizations and DFT calculations can be found in *SI Appendix, Methods and Materials*.

MD Simulations. MD simulations were performed on selected MeOH/Zn(OTf)$_2$ electrolytes. The compositions of simulated electrolytes and the lengths of NVT (constant particle number, constant volume, constant temperature) trajectories are given in *SI Appendix*, Table S3 together with the predicted transport, thermodynamic, and structural properties.

The MD simulations were performed utilizing the Tinker-HP (44) MD code with a few minor (in-house) modifications to buffer and output the stress tensor every 4 fs that was subsequently used for viscosity prediction.

A many-body AMOEBA (45) polarizable force field was used. Electrostatic interactions were represented using permanent charges, dipoles, and quadrupoles. Isotropic atomic polarizabilities were used to model induced interactions that were damped at short distances using the Thole method (46). The equations of

motion were integrated using a (bonded/nonbonded) Reference System Propagator Algorithm (RESPA) integrator with a 2 fs outer timestep (and a 0.25 fs inner timestep). The cutoff for nonbonded interactions was set to 10 Å. The screening parameter in particle-mesh Ewald was $\alpha = 0.36\ \text{Å}^{-1}$.

The force-field AMOEBA parameters for CH_3OH,[47] the initial force-field for OTf,[48] and the initial parameters for graphene [49] were taken from previous reports. The revised OTf parameters were obtained by a concomitant fit to the ab initio binding energies of ZnOTf, $Zn(OTf)_2$, OTf-MeOH and are given in *SI Appendix*, Table S6. For condensed phase simulations, the charges of Zn and OTf were decreased by 7% in order to improve agreement with conductivity for the 14:1 concentration; however, this resulted in a slightly higher degree of ion dissociation than that extracted from fits to Raman spectra. Additional MD simulations were performed in order to calculate dielectric properties for the 14:1 MeOH:$Zn(OTF)_2$ mixture at 60 °C, MeOH at 60 °C, and MeOH at 25 °C. For the mixture, 11 shorter trajectories (4.358 ns each) were generated by restarting simulations from configurations extracted from the trajectory detailed in *SI Appendix*, Table S3. Two trajectories of 2.348 ns each were generated for MeOH at 60 °C and a single trajectory of 2.739 ns was generated for MeOH at 25 °C. In all calculations, dipoles were output with a frequency of 4 fs. Dielectric spectra were calculated from the total box dipole moment autocorrelation function (*SI Appendix*, Fig. S4) for the pure MeOH and MeOH component of the 14 MeOH:$Zn(OTf)_2$ electrolyte using previously reported formalism (50). MD simulations predicted a dielectric constant of 34 for pure MeOH and 12 for the MeOH part of the 14 MeOH:$Zn(OTf)_2$ electrolyte at 60 °C.

For the electrode–electrolyte interface simulations (*SI Appendix*, Figs. S42–S44), two oppositely charged electrodes were added. Each electrode consisted of two layers of graphene. The graphene layer closest to the electrolyte had a constant charge of ±0.0088e/C and ±0.0128e/C, while the second graphene layer was uncharged. The polarization on the electrode (graphene) atoms was also represented with a point dipole using an atomic polarizability of 1 Å^{-3}.

Details on MD simulations, simulated compositions, trajectory lengths, predicted properties, and the revised OTF^- force-field parameters are given in *SI Appendix*, Tables S3 and S7.

Author affiliations: [a]Battery Science Branch, Energy Science Division, Sensor and Electron Devices Directorate, DEVCOM Army Research Laboratory, Adelphi, MD 20783; [b]Department of Mechanical Engineering and Engineering Science, The University of North Carolina at Charlotte, Charlotte, NC 28223; [c]Material, Physical and Chemical Sciences Center, Sandia National Laboratories, Albuquerque, NM 87185; [d]Department of Physics, Central Michigan University, Mount Pleasant, MI 48859; [e]Advanced Photon Source, Argonne National Laboratory, Lemont, IL 60439; [f]Department of Chemistry and Biochemistry, George Mason University, Fairfax, VA 22030; [g]Quantum Science & Engineering Center, George Mason University, Fairfax, VA 22030; and [h]Department of Chemical and Biomolecular Engineering, University of Maryland, College Park, MD 20742

1. US Geological Survey, Mineral commodity summaries 2021. https://pubs.er.usgs.gov/publication/mcs2021. Accessed 16 May 2022.
2. A. A. Yaroshevsky, Abundances of chemical elements in the Earth's crust. *Geochem. Int.* **44**, 48–55 (2006).
3. M. Winter, B. Barnett, K. Xu, Before Li ion batteries. *Chem. Rev.* **118**, 11433–11456 (2018).
4. L. E. Blanc, D. Kundu, L. F. Nazar, Scientific challenges for the implementation of Zn-ion batteries. *Joule* **4**, 771–799 (2020).
5. Y. Liang, H. Dong, D. Aurbach, Y. Yao, Current status and future directions of multivalent metal-ion batteries. *Nat. Energy* **5**, 646–656 (2020).
6. C. Li, X. Xie, S. Liang, J. Zhou, Issues and future perspective on zinc metal anode for rechargeable aqueous zinc-ion batteries. *Energy Environ. Mater.* **3**, 146–159 (2020).
7. C. Zhang et al., A ZnCl₂ water-in-salt electrolyte for a reversible Zn metal anode. *Chem. Commun. (Camb.)* **54**, 14097–14099 (2018).
8. Q. Zhang et al., Modulating electrolyte structure for ultralow temperature aqueous zinc batteries. *Nat. Commun.* **11**, 4463 (2020).
9. F. Wang et al., Highly reversible zinc metal anode for aqueous batteries. *Nat. Mater.* **17**, 543–549 (2018).
10. H. Qiu et al., Zinc anode-compatible in-situ solid electrolyte interphase via cation solvation modulation. *Nat. Commun.* **10**, 5374 (2019).
11. J. Zhao et al., "Water-in-deep eutectic solvent" electrolytes enable zinc metal anodes for rechargeable aqueous batteries. *Nano Energy* **57**, 625–634 (2019).
12. Z. Chen et al., Anion solvation reconfiguration enables high-voltage carbonate electrolytes for stable Zn/graphite cells. *Angew. Chem. Int. Ed. Engl.* **59**, 21769–21777 (2020).
13. W. Yang et al., Hydrated eutectic electrolytes with ligand-oriented solvation shells for long-cycling zinc-organic batteries. *Joule* **4**, 1557–1574 (2020).
14. L. Ma et al., Functionalized phosphonium cations enable zinc metal reversibility in aqueous electrolytes. *Angew. Chem. Int. Ed. Engl.* **60**, 12438–12445 (2021).
15. A. Naveed, H. Yang, J. Yang, Y. Nuli, J. Wang, Highly reversible and rechargeable safe Zn batteries based on a triethyl phosphate electrolyte. *Angew. Chem. Int. Ed. Engl.* **58**, 2760–2764 (2019).
16. L. Cao et al., Fluorinated interphase enables reversible aqueous zinc battery chemistries. *Nat. Nanotechnol.* **16**, 902–910 (2021).
17. Z. Li et al., Pencil drawing stable interface for reversible and durable aqueous zinc-ion batteries. *Adv. Funct. Mater.* **31**, 2006495 (2021).
18. J. Hao et al., Designing dendrite-free zinc anodes for advanced aqueous zinc batteries. *Adv. Funct. Mater.* **30**, 2001263 (2020).
19. J. F. Parker et al., Rechargeable nickel-3D zinc batteries: An energy-dense, safer alternative to lithium-ion. *Science* **356**, 415–418 (2017).
20. Q. Li et al., Calendar life of Zn batteries based on Zn anode with Zn powder/current collector structure. *Adv. Energy Mater.* **11**, 2003931 (2021).
21. L. Suo et al., "Water-in-salt" electrolyte enables high-voltage aqueous lithium-ion chemistries. *Science* **350**, 938–943 (2015).
22. J. Chen et al., Electrolyte design for LiF-rich solid–electrolyte interfaces to enable high-performance microsized alloy anodes for batteries. *Nat. Energy* **5**, 386–397 (2020).
23. L. Sheng et al., Impact of lithium-ion coordination on lithium electrodeposition. *Energy Environ. Mater.*, 10.1002/eem2.12266.
24. P. Albertus, S. Babinec, S. Litzelman, A. Newman, Status and challenges in enabling the lithium metal electrode for high-energy and low-cost rechargeable batteries. *Nat. Energy* **3**, 16–21 (2018).
25. L. Ma et al., Realizing high zinc reversibility in rechargeable batteries. *Nat. Energy* **5**, 743–749 (2020).
26. G. Bozzano, F. Manenti, Efficient methanol synthesis: Perspectives, technologies and optimization strategies. *Pror. Energy Combust. Sci.* **56**, 71–105 (2016).
27. J. M. Alía, H. G. M. Edwards, Ion solvation and ion association in lithium trifluoromethanesulfonate solutions in three aprotic solvents. An FT-Raman spectroscopic study. *Vib. Spectrosc.* **24**, 185–200 (2000).
28. L. Suo et al., "Water-in-salt" electrolyte makes aqueous sodium-ion battery safe, green, and long-lasting. *Adv. Energy Mater.* **7**, 1701189 (2017).
29. R. Buchner, G. T. Hefter, P. M. May, Dielectric relaxation of aqueous NaCl solutions. *J. Phys. Chem. A* **103**, 1–9 (1999).
30. M. S. Ding et al., Change of conductivity with salt content, solvent composition, and temperature for electrolytes of LiPF[sub 6] in ethylene carbonate-ethyl methyl carbonate. *J. Electrochem. Soc.* **148**, A1196 (2001).
31. L. Ma et al., Critical factors dictating reversibility of the zinc metal anode. *Energy Environ. Mater.* **3**, 516–521 (2020).
32. J. Banaś, K. G. Schütze, E. Heitz, Corrosion studies on zinc in a methanol/water/lithium chloride/oxygen system. *J. Electrochem. Soc.* **133**, 253–259 (1986).
33. H. G. Jenniskens, P. W. F. Dorlandt, M. F. Kadodwala, A. W. Kleyn, The adsorption of methanol on Ag(111) studied with TDS and XPS. *Surf. Sci.* **357-358**, 624–628 (1996).
34. G. Beamson, D. Briggs, *High Resolution XPS of Organic Polymers: The Scienta ESCA300 Database* (Wiley, 1992).
35. J. Duchoslav, R. Steinberger, M. Arndt, D. Stifter, XPS study of zinc hydroxide as a potential corrosion product of zinc: Rapid X-ray induced conversion into zinc oxide. *Corros. Sci.* **82**, 356–361 (2014).
36. G. Milano et al., Ionic modulation of electrical conductivity of ZnO due to ambient moisture. *Adv. Mater. Interfaces* **6**, 1900803 (2019).
37. F. Wan et al., An aqueous rechargeable zinc-organic battery with hybrid mechanism. *Adv. Funct. Mater.* **28**, 1804975 (2018).
38. M. A. Schroeder, L. Ma, G. Pastel, K. Xu, The mystery and promise of multivalent metal-ion batteries. *Curr. Opin. Electrochem.* **29**, 100819 (2021).
39. V. Petkov, RAD, a program for analysis of X-ray diffraction data from amorphous materials for personal computers. *J. Appl. Cryst.* **22**, 387–389 (1989).
40. R. Buchner, T. Chen, G. Hefter, Complexity in "simple" electrolyte solutions: Ion pairing in MgSO4(aq). *J. Phys. Chem. B* **108**, 2365–2375 (2004).

41. J. Barthel, K. Bachhuber, R. Buchner, H. Hetzenauer, Dielectric spectra of some common solvents in the microwave region. Water and lower alcohols. *Chem. Phys. Lett.* **165**, 369–373 (1990).

42. R. Raccichini, L. Furness, J. W. Dibden, J. R. Owen, N. García-Araez, Impedance characterization of the transport properties of electrolytes contained within porous electrodes and separators useful for Li-S batteries. *J. Electrochem. Soc.* **165**, A2741–A2749 (2018).

43. D. B. Shah *et al.*, Difference between approximate and rigorously measured transference numbers in fluorinated electrolytes. *Phys. Chem. Chem. Phys.* **21**, 7857–7866 (2019).

44. L. Lagardère *et al.*, Tinker-HP: A massively parallel molecular dynamics package for multiscale simulations of large complex systems with advanced point dipole polarizable force fields. *Chem. Sci. (Camb.)* **9**, 956–972 (2017).

45. J. W. Ponder *et al.*, Current status of the AMOEBA polarizable force field. *J. Phys. Chem. B* **114**, 2549–2564 (2010).

46. B. T. Thole, Molecular polarizabilities calculated with a modified dipole interaction. *Chem. Phys.* **59**, 341–350 (1981).

47. P. Ren, C. Wu, J. W. Ponder, Polarizable atomic multipole-based molecular mechanics for organic molecules. *J. Chem. Theory Comput.* **7**, 3143–3161 (2011).

48. Y.-J. Tu, Z. Lin, M. J. Allen, G. A. Cisneros, Molecular dynamics investigation of water-exchange reactions on lanthanide ions in water/1-ethyl-3-methylimidazolium trifluoromethylsufate ([EMIm][OTf]). *J. Chem. Phys.* **148**, 024503 (2018).

49. Y. Qiu, B. R. Schwegler, L.-P. Wang, Polarizable molecular simulations reveal how silicon-containing functional groups govern the desalination mechanism in nanoporous graphene. *J. Chem. Theory Comput.* **14**, 4279–4290 (2018).

50. C. Schröder, T. Sonnleitner, R. Buchner, O. Steinhauser, The influence of polarizability on the dielectric spectrum of the ionic liquid 1-ethyl-3-methylimidazolium triflate. *Phys. Chem. Chem. Phys.* **13**, 12240–12248 (2011).